Rapid Communications

Rheology of suspensions of viscoelastic spheres: Deformability as an effective volume fraction

Marco E. Rosti,[1] Luca Brandt,[1] and Dhrubaditya Mitra[2]
[1]*Linné Flow Centre and SeRC (Swedish e-Science Research Centre), KTH Mechanics, SE-100 44 Stockholm, Sweden*
[2]*NORDITA, Royal Institute of Technology and Stockholm University, Roslagstullsbacken 23, SE-106 91 Stockholm, Sweden*

(Received 14 September 2017; published 22 January 2018)

We study suspensions of *deformable* (viscoelastic) spheres in a Newtonian solvent in plane Couette geometry, by means of direct numerical simulations. We find that in the limit of vanishing inertia, the effective viscosity μ of the suspension increases as the volume fraction occupied by the spheres Φ increases and decreases as the elastic modulus of the spheres G decreases; the function $\mu(\Phi,G)$ collapses to a universal function $\mu(\Phi_e)$ with a reduced effective volume fraction $\Phi_e(\Phi,G)$. Remarkably, the function $\mu(\Phi_e)$ is the well-known Eilers fit that describes the rheology of suspension of *rigid* spheres at all Φ. Our results suggest different ways to interpret the macrorheology of blood.

DOI: 10.1103/PhysRevFluids.3.012301

Most of the fluids we encounter in our everyday life—from the mud we wade through to the blood that flows through our veins—are complex fluids. One of the most useful ways to understand the rheology of complex fluids is to model them as suspensions of objects in a Newtonian solvent with dynamic viscosity μ_f and density ρ_f [1,2]. The rheology of suspensions can be quite complex, as it depends on the shear rate $\dot{\gamma}$, the volume fraction Φ occupied by the suspended objects, the properties of the suspended objects themselves (some examples are rigid spheres, bubbles, a different fluid enclosed in a membrane), and their polydispersity. In the simplest case of rigid spheres in the limit of small Φ, and vanishing inertia (small $\dot{\gamma}$), also ignoring thermal fluctuations (infinite Peclet number), the fractional increase in the effective viscosity of the suspension is given by (see, e.g., Ref. [3], Sec. 4.11)

$$\frac{\mu}{\mu_f} = 1 + \frac{5}{2}\Phi + O(\Phi^2). \tag{1}$$

At present there is no theory that allows us to calculate μ for any given Φ and $\dot{\gamma}$. Different empirical formulas provide a good description of the existing experimental and numerical results [4–7]. Among those, we consider here the Eilers formula [1,2],

$$\frac{\mu}{\mu_f} = \left[1 + B\frac{\Phi}{1-\Phi/\Phi_m}\right]^2, \tag{2}$$

which fits well the experimental and numerical data [5,6] for both low and high values of Φ, up to about 0.6. In the expression above, Φ_m is the geometrical maximum packing fraction, and B is a constant, and the best fit to the data yields $\Phi_m = 0.58$–0.63 and $B = 1.25$–1.7. If the radius R of the spheres and the shear rate are large enough, the particle Reynolds number, defined as $\mathrm{Re} \equiv (\rho_f R^2 \dot{\gamma})/\mu_f$, is greater than unity, inertial effects are non-negligible, and the viscosity $\mu = \mu(\Phi,\mathrm{Re})$. Remarkably, direct numerical simulations (DNSs) in Ref. [8] demonstrated that the Eilers fit is a good approximation even for inertial suspensions if Φ in Eq. (2) is replaced by an *increased effective volume fraction*

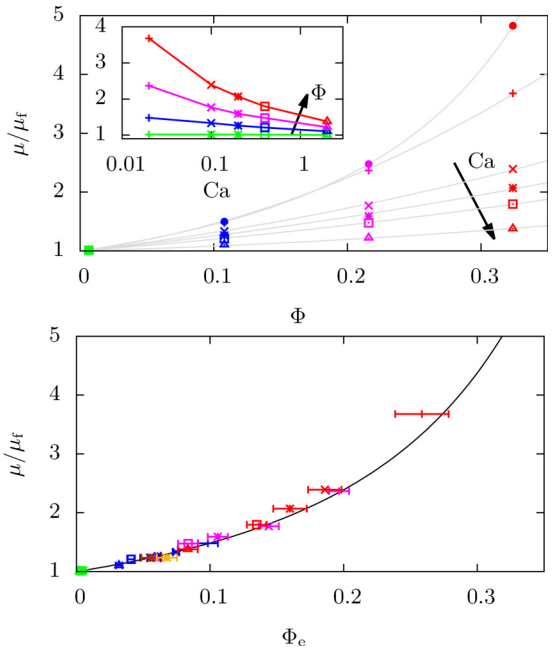

FIG. 1. Top: The fractional increase in effective viscosity μ/μ_f as a function of the volume fraction Φ for several different values of the capillary numbers Ca = 0.02 (+), 0.1 (×), 0.2 (∗), 0.4 (□), and 2 (△). All the cases have $K = 1$. For comparison we also plot the same data for rigid particles [8] [Ca = 0 (•)]. The inset shows the same data replotted as a function of Ca for different $\Phi \approx 0.0016$ (green), 0.11 (blue), 0.22 (magenta), and 0.33 (red). Bottom: The same data replotted as a function of effective volume fraction Φ_e collapses to a universal function given by the Eilers fit, Eq. (2), with $\Phi_m = 0.6$ and $B = 1.7$. The horizontal error bars show the standard deviation of the effective volume fraction. In the figure we also show the fitted data for three more cases at $\Phi = 0.11$, Ca = 0.2, and viscosity ratio $K = 0.01$ (black), 0.1 (brown), and 10 (orange). The interested reader is referred to the Supplemental Material [16] for a discussion of the effect of K on the effective viscosity.

$\Phi_e(\Phi,\mathrm{Re})$. Due to the increase of the effective volume fraction with the applied shear, the suspension viscosity increases, a phenomenon called inertial shear thickening.

In this Rapid Communication we add a different complexity to this problem, one that is particularly important to understand the rheology of biological flows; while keeping small Re, we allow the suspended particles to be *deformable*. In particular, we model the spheres as viscoelastic material with an elastic shear modulus G and viscosity μ_s. Thereby we introduce two different dimensionless parameters: the capillary number $\mathrm{Ca} \equiv \mu_f \dot{\gamma}/G$ and the viscosity ratio $K \equiv \mu_s/\mu_f$. This problem has a long history starting with the work by Taylor [9] who assumed a small deformation (Ca → 0), and showed that for small Φ, the coefficient of the linear term on the right-hand side of Eq. (1) is $(5K + 2)/(2K + 2)$. Later analytical calculations [10–14] attempted to extend the result of Taylor to higher order in Φ and Ca using perturbative expansions. Recently, numerical simulations [15] have been used to estimate the deformation and suspension viscosity for elastic capsules.

We use direct numerical simulations (DNSs) of deformable spheres in plane Couette flow to calculate $\mu(\Phi,\mathrm{Ca})$, for a wide range of Φ (up to ≈33%) and Ca (0.02–2). We find that μ increases as Φ increases and decreases as Ca increases, i.e., we find shear thinning due to deformability. More importantly, the function $\mu(\Phi,\mathrm{Ca})$ collapses to a universal function $\mu(\Phi_e)$ (see Fig. 1), with a *reduced effective volume fraction* $\Phi_e(\Phi,\mathrm{Ca})$. Here, Φ_e is not a fit parameter, but found independently from the shape of the deformed particles in the suspensions. Remarkably, the function $\mu(\Phi_e)$ is well

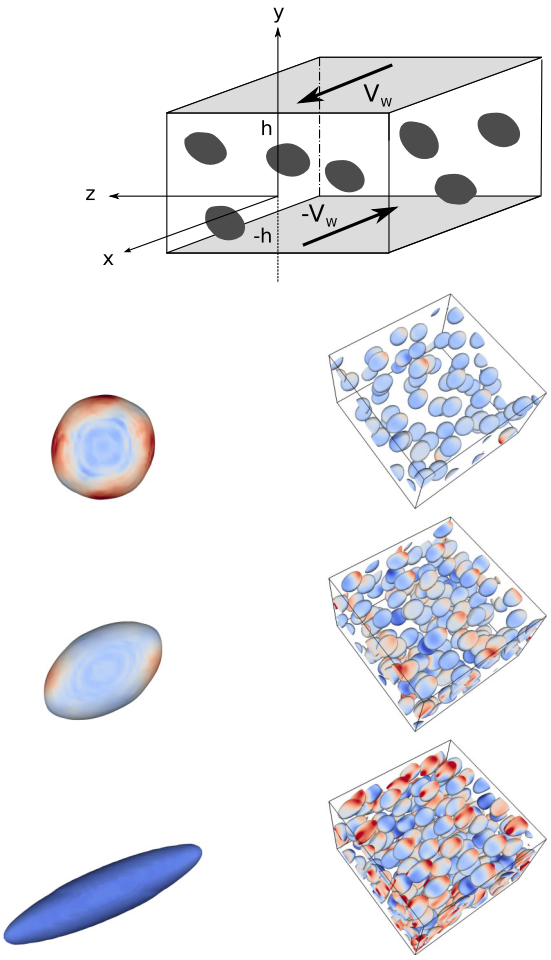

FIG. 2. Top: Sketch of the channel geometry. The top and bottom walls, located at $y = \pm h$, move with opposite velocities $\pm V_w$ in the streamwise x direction. Left: Shape of the deformed particle for lowest Φ (just a single object in the computational box) for three different capillary numbers, Ca = 0.02, 0.2, and 2. Right: Shape of the deformed particles at Ca = 0.2 for three different volume fractions, $\Phi = 0.11$, 0.22, and 0.33. The intensity of color shows B^{12}. In all our simulations we use Re = 0.1 with several different values of $\Phi \approx 0.0016$, 0.11, 0.22, and 0.33, and Ca = 0.02, 0.1, 0.2, 0.4, and 2. We use the viscosity ratio $\mu_s/\mu_f = 1$ for all our simulations, except for three more cases with $\phi = 0.11$ and Ca = 0.2, where $\mu_s/\mu_f = 0.01$, 0.1, and 10.

described by the Eilers fit, Eq. (2). This demonstrates a striking universality of complex fluids: The Eilers fit works for non-Brownian inertialess suspensions of rigid objects, suspensions at moderate Re, and also for non-Brownian suspensions of deformable objects, provided one uses Φ_e instead of Φ.

We perform DNS in the plane Couette geometry—see Fig. 2 for a sketch of our computational box. The *deformable* spheres suspended in the Newtonian fluid are modeled with a two-phase approach: The local volume fraction is denoted by ϕ, i.e., $\phi = 1$ inside the viscoelastic solid phase and $\phi = 0$ in the fluid phase, with a sharp boundary in between; hence $\Phi = \langle\phi\rangle$, where $\langle\cdot\rangle$ denotes the volume average [17]. The incompressible Navier-Stokes equations are solved everywhere for a monolithic

velocity field [18–20] $\boldsymbol{u}$ and a stress tensor σ^{ij} given by

$$\sigma^{ij} = \phi\sigma_{\rm s}^{ij} + (1-\phi)\sigma_{\rm f}^{ij}, \tag{3a}$$

$$\sigma_{\rm s}^{ij} = -p\delta^{ij} + 2\mu_{\rm s}D^{ij} + GB^{ij}, \tag{3b}$$

$$\sigma_{\rm f}^{ij} = -p\delta^{ij} + 2\mu_{\rm f}D^{ij}. \tag{3c}$$

Here, the suffixes f and s indicate the fluid and solid phase, $D^{ij} \equiv (1/2)(\partial^i u^j + \partial^j u^i)$ the rate-of-strain tensor, p the pressure, and δ^{ij} the Kronecker delta. Clearly the fluid phase is a Newtonian one with dynamic viscosity $\mu_{\rm f}$ and the solid phase is both viscous ($\mu_{\rm s}$) and hyperelastic with the left Cauchy-Green tensor B^{ij}. Both ϕ and B^{ij} are conserved quantities advected by the local velocity $\boldsymbol{u}$.

The dynamical equations are solved using a second-order finite-difference scheme in space and a third-order Runge-Kutta scheme in time. The pressure is obtained by solving the Poisson equation using Fourier transforms. We use a Cartesian uniform mesh in a rectangular box of size $16R \times 10R \times 16R$, with 16 grid points per particle radius R. Periodic boundary conditions are imposed in the streamwise x and spanwise z directions and no-slip conditions at the walls located at $y = -h$ and $y = h$, with y the wall-normal direction, which move in opposite directions with a constant streamwise velocity $\pm V_{\rm w} = h\dot{\gamma}$. We have validated our code by reproducing the results of Ref. [21], and details of our implementation can be found in Ref. [22]. An additional validation can be found in the Supplemental Material [16] where we compare our results with Ref. [23]. We have checked that doubling the resolution in all directions results in an insignificant (less than 0.5%) change in the results. Also, the size of the domain has been chosen sufficiently large to avoid confinement effects [8,24]. The list of parameters investigated is given in the caption of Fig. 2.

We first run a set of simulations with the smallest $\Phi \approx 0.0016$ which corresponds to one sphere in the computational volume. After the transients die out, the sphere deforms to approximately an ellipsoid. Examples are shown in Fig. 2, left column, for three different values of Ca. We characterize these shapes by the Taylor parameter [9],

$$\mathcal{T} = \frac{b-a}{b+a}, \tag{4}$$

where b and a are the lengths of the semimajor and semiminor axis in the shear xy plane. For higher values of Φ, we start our DNS with the spheres randomly distributed in the computational domain and then wait until $T_{\rm tr} = 20/\dot{\gamma}$ to reach a statistical stationary state [25]. Typical snapshots of the suspensions are shown in Fig. 2, right column, for three different values of Φ. We calculate $\mathcal{T}$ by averaging over all the ellipsoids and plot $\mathcal{T}(\Phi,\mathrm{Ca})$ in Fig. 3. We also show the results of the perturbative analysis of Ref. [12], which, as expected, agrees with our results at small Ca and small Φ, and results from the numerical simulations of single particles in a box in Refs. [26–28].

We calculate the effective viscosity $\mu(\Phi,\mathrm{Ca})$ as the ratio between the shear stress at the walls and $\dot{\gamma}$. The effective viscosity μ, normalized by $\mu_{\rm f}$, as a function of Φ for several different values of Ca and as a function of Ca for several different values of Φ, is shown in Fig. 1. Clearly, for a fixed Ca, the effective viscosity increases with Φ, whereas for a fixed Φ, the effective viscosity decreases as the capillary number increases. The increase of Ca can, on one hand, be interpreted as a decrease in G (with $\dot{\gamma}$ and $\mu_{\rm f}$ held constant), i.e., μ decreases as the spheres become more deformable. On the other hand, the increase of Ca can be interpreted as an increase of $\dot{\gamma}$ (with G and $\mu_{\rm f}$ held constant), consequently μ decreases as $\dot{\gamma}$ increases, i.e., we observe shear thinning. This latter interpretation is valid only when the inertial effects remain vanishingly small. This is consistent with earlier studies [13,25] for small Ca and Φ (for a demonstration, see the Supplemental Material [16]).

At constant Φ, as Ca increases, $\mathcal{T}$ increases and the spheres become approximately prolate spheroids aligned with the shear directions [15]. This suggests that the shear thinning (decrease in μ) with increasing Ca can be interpreted in terms of a decrease in the *effective* volume fraction $\Phi_{\rm e}$, a concept successfully used in the past for suspensions with different properties, such as charged colloidal particles, fiber and platelet suspensions, and polyelectrolyte solutions [2,29–31]. Here, we

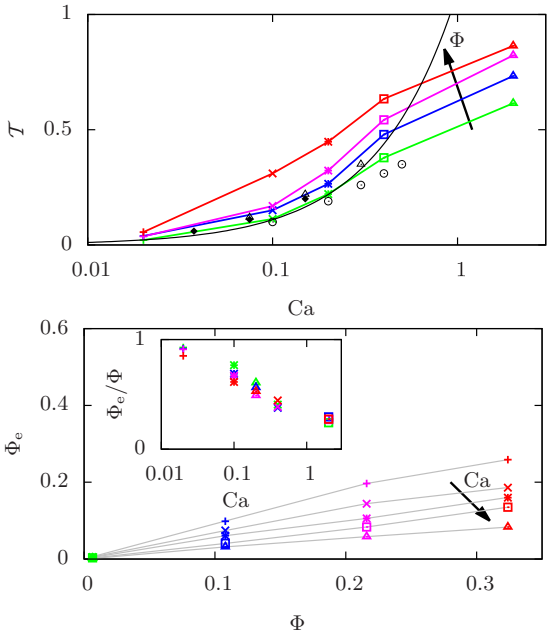

FIG. 3. Top: The Taylor deformation parameter $\mathcal{T}$ Eq. (4) as a function of capillary number Ca = 0.02 (+), 0.1 (×), 0.2 (∗), 0.4 (⊡), and 2 (△) for $\Phi \approx 0.0016$ (green), 0.11 (blue), 0.22 (magenta), and 0.33 (red). All the cases have $K = 1$. The black solid line shows the result of the perturbative calculation of Ref. [12] expected to hold for small Ca and Φ. The black symbols are numerical results from the literature for a single particle in a box. In particular, the triangle and rhombus are the results from Refs. [26,27] which were calculated for $\Phi \approx 0.06$, while the circle the two-dimensional simulation from Ref. [28] with $\Phi \approx 0.05$. Bottom: The effective volume fraction Φ_e as a function of the volume fraction Φ. The inset shows Φ_e/Φ as a function of the capillary number Ca, with logarithmic scale for the x axis.

define it by $\Phi_e = (4\pi/3)\langle a\rangle^3/\mathcal{V}$, where $\langle a\rangle$ is the mean semiminor axis of all the particles calculated from the DNS and $\mathcal{V}$ the total volume of the computational box. We use the variance of a to estimate the error in Φ_e. The choice of using the minor axis is different from what was done in previous works for fiber suspensions [32–34], where the major axis is usually considered. This is motivated by the fact that in our case the particles are not tumbling and are approximately aligned with the mean shear direction, thus, what matters is the dimension in the direction normal to the mean shear, i.e., the minor axis. The reduced volume fraction Φ_e increases with Φ and decreases with Ca [see Fig. 3(bottom)]. Furthermore, we find that Φ_e/Φ is a function of Ca alone [see the inset of Fig. 3(bottom)], a finding useful for future modeling. This brings us to the central result of this Rapid Communication in Fig. 1(bottom): The effective viscosity μ/μ_f plotted as a function of Φ_e for all the different cases collapses to a universal function, i.e., we have shown that the effect of the deformability of the particles can be included into the effective viscosity of the suspension as follows,

$$\mu/\mu_f = \mathcal{F}[\Phi_e(\Phi,\mathrm{Ca})], \tag{5}$$

where Φ_e is the effective volume fraction encoding the deformation, and $\mathcal{F}$ a universal function. Remarkably, we find that the Eilers fit, Eq. (2), with Φ replaced by Φ_e provides a good description of this universal function. Data for four different values of the viscosity ratio K are included in Fig. 1(bottom), which also collapse to the universal Eilers fit. As shown in the Supplemental Material [16], we find that μ/μ_f depends weakly on the viscosity ratio K. The data from another recent DNS [15] of fluid-filled deformable capsules can also be collapsed to the universal Eilers fit; see the Supplemental Material [16].

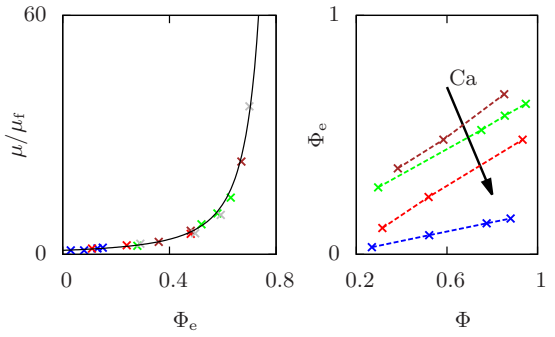

FIG. 4. Left: The effective viscosity of suspensions of RBCs for different deformabilities and viscosity ratio plotted as a function of the effective volume fraction collapses to the Eilers fit. The data are obtained from Fig. 5 of Ref. [35]. The brown points correspond to normal RBCs in saline, while the blue, red, and green ones to RBCs in dextran solutions of viscosities 3.2, 11, and 67 cP, respectively. The gray symbols are the rigid RBCs treated with acetylaldehyde. Right: The effective volume fraction Φ_e as a function of Φ necessary to obtain the collapse in the left panel.

Finally, we demonstrate how robust our results are by applying them to *experimental* data [35] on the viscosity of suspensions of red blood cells (RBCs)—to distinguish such a suspension from blood, which is a more complex system, we call [36] them erythrocite suspensions (ESs). Although several experiments have measured the effective viscosity of erythrocite suspensions under a range of volume fractions and shear rates (see, e.g., Refs. [37,38] for a recent review of numerical and experimental results), only Ref. [35] measured the effective viscosity at four different capillary numbers too by changing the viscosity μ_f of the solvent [39], and compared it against one rigid case obtained by treating the RBCs with acetaldehyde. To apply our result to these data we first fit the Eilers formula to the case of the hard RBCs, obtaining $B = 1.25$ and a maximum packing fraction $\Phi_m = 0.88$, as the undeformed shape of the RBCs is not spherical but disklike [40]. With these changes we find that the viscosity of RBCs can be collapsed to the Eilers fit, as shown in Fig. 4(left). As a necessary condition for this collapse we obtain the dependence of the effective volume fraction Φ_e with Φ shown in Fig. 4(right). The curves are approximately linear, and decrease with Ca for a fixed Φ, which is similar to what we have obtained from our simulations [Fig. 3(bottom)]. As various diseases, including malaria and sickle cell anemia, increase the deformability of RBCs, our results suggests the intriguing possibility that it may also be possible to use our method to model the change in the effective viscosity of blood in such cases [41].

To conclude, our simulations show that a suspension of deformable incompressible spheres in a Newtonian fluid displays shear thinning and that this can be understood in terms of a reduction of the effective volume fraction occupied by the suspended spheres due to their deformation. Considered in conjunction with earlier results [8], we find that the Eilers fit used with the concept of effective volume fraction is a surprising powerful too to interpret rheological data. In other words, the suspension dynamics is mainly determined by excluded volume effects for non-Brownian suspensions of rigid and deformable particles, the former also in the weakly inertial regime. A word of caution though, in that not all aspects of non-Brownian suspensions can be described by an effective viscosity, e.g., a laminar to turbulent transition in a suspension is qualitatively different from that of a Newtonian fluid [42]. In view of our initial success in interpreting existing rheological measurements of suspensions of RBCs, we suggest a systematic experimental investigation of suspensions of cells and capsules with different deformabilities.

The work of M.E.R. and L.B. was supported by the European Research Council Grant No. ERC-2013-CoG-616186, TRITOS, and by the Swedish Research Council (Grant No. VR 2014-5001). D.M. is supported by grants from the Swedish Research Council (Grants No. 638-2013-9243 and

No. 2016-05225). The authors acknowledge computer time provided by SNIC (Swedish National Infrastructure for Computing).

[1] J. J. Stickel and R. L. Powell, Fluid mechanics and rheology of dense suspensions, Annu. Rev. Fluid Mech. **37**, 129 (2005).
[2] J. Mewis and N. J. Wagner, *Colloidal Suspension Rheology* (Cambridge University Press, Cambridge, UK, 2012).
[3] G. K. Batchelor, *An Introduction to Fluid Dynamics* (Cambridge University Press, Cambridge, UK, 2000).
[4] F. Ferrini, D. Ercolani, B. De Cindio, L. Nicodemo, L. Nicolais, and S. Ranaudo, Shear viscosity of settling suspensions, Rheol. Acta **18**, 289 (1979).
[5] I. E. Zarraga, D. A. Hill, and D. T. Leighton, Jr., The characterization of the total stress of concentrated suspensions of noncolloidal spheres in Newtonian fluids, J. Rheol. **44**, 185 (2000).
[6] A. Singh and P. R. Nott, Experimental measurements of the normal stresses in sheared Stokesian suspensions, J. Fluid Mech. **490**, 293 (2003).
[7] P. M. Kulkarni and J. F. Morris, Suspension properties at finite Reynolds number from simulated shear flow, Phys. Fluids **20**, 040602 (2008).
[8] F. Picano, W. P. Breugem, D. Mitra, and L. Brandt, Shear Thickening in Non-Brownian Suspensions: An Excluded Volume Effect, Phys. Rev. Lett. **111**, 098302 (2013).
[9] G. I. Taylor, The viscosity of a fluid containing small drops of another fluid, Proc. R. Soc. London, Ser. A **138**, 41 (1932).
[10] R. G. Cox, The deformation of a drop in a general time-dependent fluid flow, J. Fluid Mech. **37**, 601 (1969).
[11] N. A. Frankel and A. Acrivos, The constitutive equation for a dilute emulsion, J. Fluid Mech. **44**, 65 (1970).
[12] S. J. Choi and W. R. Schowalter, Rheological properties of nondilute suspensions of deformable particles, Phys. Fluids **18**, 420 (1975).
[13] R. Pal, Viscous behavior of concentrated emulsions of two immiscible Newtonian fluids with interfacial tension, J. Colloid Interface Sci. **263**, 296 (2003).
[14] T. Gao, H. H. Hu, and P. P. Castañeda, Shape Dynamics and Rheology of Soft Elastic Particles in a Shear Flow, Phys. Rev. Lett. **108**, 058302 (2012).
[15] D. Matsunaga, Y. Imai, T. Yamaguchi, and T. Ishikawa, Rheology of a dense suspension of spherical capsules under simple shear flow, J. Fluid Mech. **786**, 110 (2016).
[16] See Supplemental Material at http://link.aps.org/supplemental/10.1103/PhysRevFluids.3.012301 for the validation of our code and further analysis of our fit with literature results.
[17] A similar approach gives rise to the Navier-Stokes-Cahn-Hilliard equations in binary fluids.
[18] G. Tryggvason, M. Sussman, and M. Y. Hussaini, Immersed boundary methods for fluid interfaces, in *Computational Methods for Multiphase Flow*, edited by A. Prosperetti and G. Tryggvason (Cambridge University Press, Cambridge, UK, 2009), Vol. 3, p. 37.
[19] S. Takeuchi, Y. Yuki, A. Ueyama, and T. Kajishima, A conservative momentum-exchange algorithm for interaction problem between fluid and deformable particles, Int. J. Numer. Methods Fluids **64**, 1084 (2010).
[20] M. Quintard and S. Whitaker, Transport in ordered and disordered porous media II: Generalized volume averaging, Transp. Porous Media **14**, 179 (1994).
[21] K. Sugiyama, S. Ii, S. Takeuchi, S. Takagi, and Y. Matsumoto, A full Eulerian finite difference approach for solving fluid-structure coupling problems, J. Comput. Phys. **230**, 596 (2011).
[22] M. E. Rosti and L. Brandt, Numerical simulation of turbulent channel flow over a viscous hyper-elastic wall, J. Fluid Mech. **830**, 708 (2017).
[23] M. M. Villone, M. A. Hulsen, P. D. Anderson, and P. L. Maffettone, Simulations of deformable systems in fluids under shear flow using an arbitrary Lagrangian Eulerian technique, Comput. Fluids **90**, 88 (2014).
[24] W. Fornari, L. Brandt, P. Chaudhuri, C. U. Lopez, D. Mitra, and F. Picano, Rheology of Confined Non-Brownian Suspensions, Phys. Rev. Lett. **116**, 018301 (2016).

[25] P. Srivastava, A. R. Malipeddi, and K. Sarkar, Steady shear rheology of a viscous emulsion in the presence of finite inertia at moderate volume fractions: Sign reversal of normal stress differences, J. Fluid Mech. **805**, 494 (2016).
[26] C. Pozrikidis, Finite deformation of liquid capsules enclosed by elastic membranes in simple shear flow, J. Fluid Mech. **297**, 123 (1995).
[27] C. D. Eggleton and A. S. Popel, Large deformation of red blood cell ghosts in a simple shear flow, Phys. Fluids **10**, 1834 (1998).
[28] S. Ii, K. Sugiyama, S. Takeuchi, S. Takagi, and Y. Matsumoto, An implicit full Eulerian method for the fluid-structure interaction problem, Int. J. Numer. Methods Fluids **65**, 150 (2011).
[29] J. Mewis, W. J. Frith, T. A. Strivens, and W. B. Russel, The rheology of suspensions containing polymerically stabilized particles, AIChE J. **35**, 415 (1989).
[30] W. J. Frith, P. d'Haene, R. Buscall, and J. Mewis, Shear thickening in model suspensions of sterically stabilized particles, J. Rheol. **40**, 531 (1996).
[31] D. Quemada, Rheological modeling of complex fluids. I. The concept of effective volume fraction revisited, Eur. Phys. J.: Appl. Phys. **1**, 119 (1998).
[32] G. K. Batchelor, The stress generated in a non-dilute suspension of elongated particles by pure straining motion, J. Fluid Mech. **46**, 813 (1971).
[33] R. J. Kerekes, Rheology of fibre suspensions in papermaking: An overview of recent research, Nord. Pulp Pap. Res. J. **21**, 598 (2006).
[34] F. Lundell, L. D. Söderberg, and P. H. Alfredsson, Fluid mechanics of papermaking, Annu. Rev. Fluid Mech. **43**, 195 (2011).
[35] L. Dintenfass, Internal viscosity of the red cell and a blood viscosity equation, Nature (London) **219**, 956 (1968).
[36] D. A. Fedosov, W. Pan, B. Caswell, G. Gompper, and G. E. Karniadakis, Predicting human blood viscosity in silico, Proc. Natl. Acad. Sci. USA **108**, 11772 (2011).
[37] R. G. Winkler, D. A. Fedosov, and G. Gompper, Dynamical and rheological properties of soft colloid suspensions, Curr. Opin. Colloid Interface Sci. **19**, 594 (2014).
[38] A. Yazdani, X. Li, and G. E. Karniadakis, Dynamic and rheological properties of soft biological cell suspensions, Rheol. Acta **55**, 433 (2016).
[39] The viscosity ratio K changes too, but our results show that the μ does not depend strongly on K.
[40] S. Mueller, E. W. Llewellin, and H. M. Mader, The rheology of suspensions of solid particles, Proc. R. Soc. London, Ser. A **466**, 1201 (2010).
[41] This applies to macrorheology of blood not microrheology which deals with blood flows in capillaries of sizes close the size of the RBCs themselves.
[42] I. Lashgari, F. Picano, W. P. Breugem, and L. Brandt, Laminar, Turbulent, and Inertial Shear-Thickening Regimes in Channel Flow of Neutrally Buoyant Particle Suspensions, Phys. Rev. Lett. **113**, 254502 (2014).